Density functional theory calculations of the bandstructure of cubic boron arsenide☆

A. King [a,d] [ID],*, R. Gillen [b] [ID], G. Burwell [c,d], B.A. Niyikiza [e], F.J. Pan [e], Z.F. Ren [e], L. Li [b,d], K. Kalna [a,d] [ID]

[a] *Nanoelectronic Devices Computational Group, Department of Electronic & Electrical Engineering, Faculty of Science & Engineering, Swansea University, Swansea, SA1 8EN, Wales, United Kingdom*
[b] *Department of Electronic & Electrical Engineering, Faculty of Science & Engineering, Swansea University, Swansea, SA1 8EN, Wales, United Kingdom*
[c] *Department of Physics, Faculty of Science & Engineering, Swansea University, Swansea, SA1 8EN, Wales, United Kingdom*
[d] *Centre for Integrative Semiconductor Materials, Faculty of Science & Engineering, Swansea University, Swansea, SA1 8EN, Wales, United Kingdom*
[e] *Department of Physics and Texas Center for Superconductivity, University of Houston, Houston, TX 77204, United States*

ARTICLE INFO

ABSTRACT

A bandgap of cubic boron arsenide (cBAs) is systematically calculated using various approaches in density functional theory (DFT). We explore how basis set, atomic potential, exchange–correlation functional, and spin–orbit coupling influence the bandgap calculations when using Synopsis QuantumATK (QATK), Quantum ESPRESSO, and VASP codes. Our measurements of indirect and direct bandgaps serve as reference values. We found that using a linear combination of atomic orbitals (LCAO) with an ultra basis set, Pseudo-Dojo norm-conserving pseudopotentials, the HSE06 hybrid exchange–correlation functional, and non-collinear spin–orbit coupling (NSOC) in QATK DFT calculations yields indirect and direct bandgaps of 2.03 eV and 3.99 eV, which are very close to our measurements of 2.01 eV and 4.24 eV, and recent experimental results of 2.02 eV and 4.12 eV, respectively. NSOC is critical for accurate bandstructure calculations in relatively wide bandgap materials, and the HSE06 functional and optimised PseudoDojo pseudopotentials play a similar role. Using the more common generalised gradient approximation (GGA) exchange–correlation functional PBE underestimates the indirect and direct bandgaps, with values ranging from 1.13 eV to 1.36 eV and from 3.04 eV to 3.37 eV, respectively, depending on the type of basis set, potential, and spin–orbit coupling used.

1. Introduction

Cubic boron arsenide (cBAs) has recently emerged as a semiconductor material with the potential to overcome the limitations of other semiconductor materials [1,2] when implemented in critical components in semiconductor technology. These limitations often include: (i) a large difference between electron and hole mobility as in Si, Ge, or GaAs, making the operation of CMOS logic [3,4] or power inverters and converters cumbersome [5], (ii) a small bandgap but a very high electron mobility as in InP or InSb [6] resulting in early impact ionisation [7,8], or (iii) a small thermal conductivity, such as in GaN [9] or β-Ga$_2$O$_3$ [10], leading to substantial challenges in removing dissipated heat during device operations. On the contrary, cBAs exhibits comparable electron (1400 cm^2 V^{-1} s^{-1}) and hole mobility (2100 cm^2

V^{-1} s^{-1}) [11], offers a relatively large bandgap [12], and has a very high thermal conductivity (1300 W m^{-1} K^{-1}), which is only surpassed by diamond. These exceptional material properties position cBAs as an ideal semiconductor, perfectly suited for CMOS logic, power handling, switching power device, and for a wide range of acoustic and sensing applications.

Accurate knowledge of a semiconductor material bandgap is vital for the design of semiconductor devices. The bandgap of a semiconductor affects in various device figures of merit such as device breakdown, on-resistance, carrier mobility, saturation velocity, gate leakage, band-to-band tunnelling, Schottky–Read–Hall recombination, optical efficiency, light sensitivity, among others. Therefore, the accurate calculation and experimental determination of the bandgap of cBAs is crucial for the further development of cBAs-based devices and

---

architectures. Unintentional energy states within the bandgap, created during fabrication, can distort the bandgap making it smaller. While various techniques can measure the material bandgap, first-principle calculations like Density Functional Theory (DFT) offer a powerful approach to determine the bandgap and bandstructure of cBAs. However, the DFT literature does not even agree on the bandgap for cBAs, ranging from 0.98 eV [13] to 2.05 eV [14].

In this work, we carry out systematic DFT calculations, studying various basis sets, exchange–correlation functionals, and spin–orbit coupling (SOC) approximations using three DFT codes: Synopsis QuantumATK (QATK) [15], Quantum ESPRESSO (QESP) [16], and Vienna Ab-initio Simulation Package (VASP) [17,18]. Since DFT is based on the principle that the electronic bandstructure of a material can be calculated by approximating the many-body electron system through its electron density within a one-electron framework, the remaining many-body effects must be incorporated into an exchange–correlation functional [19]. Consequently, the form of the exchange–correlation functional often plays a crucial role in the accuracy of the DFT calculations [20]. The accurate band structure requires knowledge of the quasiparticle spectrum and electronic excitations [19] derived from the exact exchange–correlation functional [20,21] or many-body perturbation theory [22], which are extremely demanding to compute accurately. This usually necessitates a trade-off between accuracy and affordable computational complexity. Therefore, computationally efficient DFT methods that offer accurate total energies and bandgaps are of great interest for the simulations of phenomena such as defect formation energies. Local approximations to the exact exchange–correlation functional such as the Local Density Approximation (LDA) or the Generalised Gradient Approximation (GGA) have been established as time-tested workhorses for the efficient simulation of structural and vibrational properties of semiconductors. However, these local approximations are smooth functions of the electron density and lack the derivative discontinuities present in the exact functional [20], which often leads to a systematic underestimation of material bandgaps [23]. Derivative discontinuities can be incorporated into DFT frameworks either empirically or enforcing known constraints. For example, certain meta-GGA functionals partially achieve this by including the kinetic energy density [24]. A popular alternative approach is offered by hybrid functionals [25,26]. Since Hartree–Fock exchange represents the exact exchange for one-electron systems, it displays the desired derivative discontinuity, which is inherited by hybrid functionals containing a fraction of Hartree–Fock exchange [27]. While being a typical method of choice for DFT-based simulations of electronic properties, the increased computational complexity has to be balanced against gains in accuracy for applications on larger systems.

Therefore, our objective is to determine the best DFT methodology to calculate indirect and direct bandgap energies. The calculated bandgap is compared against our indirect and direct bandgap measurements of 2.01 eV and 4.24 eV, respectively, as well as the recent experimental values of 2.02 eV and 4.12 eV [28], which all serve as a reference. We find that the most accurate calculated bandgap is obtained by using the linear combination of atomic orbitals (LCAO) with an ultra basis set, a lattice constant of 4.777 Å, a **k**-point grid of $10 \times 10 \times 10$, the hybrid Heyd–Scuseria–Ernzerhof functional HSE06 [29], optimised norm-conserving Pseudo-Dojo pseudopotentials for both boron and arsenic, and a wave function cut-off energy of 1088 eV. This calculation approach yield indirect and direct bandgaps of 2.03 eV and 3.99 eV, which perfectly match our and reported experimental data [28] obtained from the ultraviolet–visible-near infrared (UV–Vis-NIR) spectroscopy [30].

2. Density functional theory approximations

DFT calculations are performed using the Synopsis QATK DFT software, as well as two open source DFT codes, QESP and VASP. A supercell of cBAs is illustrated in Fig. 1. The QATK calculations utilise
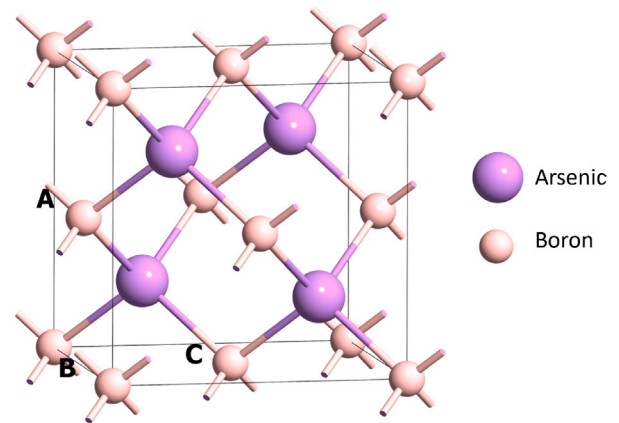

Fig. 1. Supercell of the face-centred cBAs.
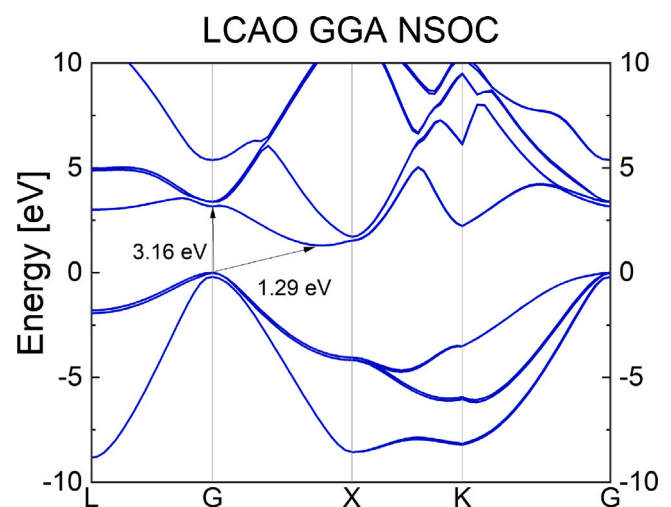

Fig. 2. Bandstructure of cBAs obtained from QATK, calculated using the LCAO with a medium basis set, the Pseudo-Dojo pseudopotential, the GGA.PBA functional, and non-collinear SOC (NSOC).
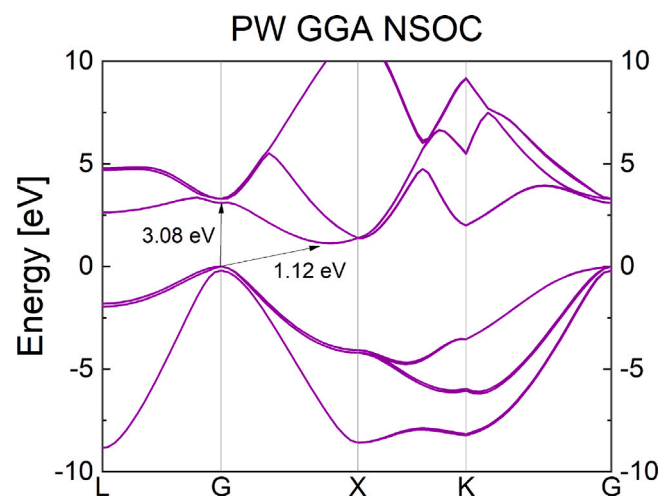

Fig. 3. Bandstructure of cBAs obtained from QATK using the PW with a medium basis set, the Pseudo-Dojo pseudopotential, the GGA.PBA functional, and non-collinear SOC (NSOC).

Table 1

Indirect and direct bandgaps of cBAs obtained from QATK and QESP comparing the listed DFT calculation approaches. The spin–orbit coupling (SOC) is always non-collinear. LCAO (m) and (u) refer to medium and ultra basis sets of the linear combination of atomic orbitals, Pseudo-Dojo stands for optimised norm-conserving pseudopotentials, and PAW for the projector augmented-wave method. PBE stands for the Perdew–Burke–Ernzerhof functional, HSE for the Heyd–Scuseria–Ernzerhof functional, mGGA for the TASK meta-generalised gradient approximation (meta-GGA), which also includes kinetic energy density, and GGA for the generalised gradient approximation. PBE+GW refers to the Perdew–Burke–Ernzerhof (PBE) exchange–correlation functional with self-energy corrections obtained from a Green function (G) and screened Coulomb interaction (W) approach (GW).

DFT code	Basis set	Potential	Functional	Exchange-Correlation potential	Indirect bandgap [eV]	Direct bandgap [eV]
QATK	LCAO (m)	Pseudo-Dojo	PBE	GGA	1.29	3.16
	LCAO (m)		HSE06	Hybrid	2.16	4.05
	LCAO (u)		HSE06	Hybrid	2.03	3.99
QATK	Plane Wave	Pseudo-Dojo	PBE	GGA	1.13	3.08
			HSE06	Hybrid	1.97	3.97
		PAW	PBE	GGA	1.13	3.04
QESP	Plane Wave	Pseudo-Dojo	mGGA	GGA	1.81	3.43
			PBE+GW	GGA	2.11	4.14

a model with a unit cell of 2 atoms, a space group of F-43 m, a lattice constant of 4.777 Å, and a **k**-point grid of $10 \times 10 \times 10$. Within the QATK DFT software, we are exploring various basis sets: the linear combination of atomic orbitals (LCAO) with medium and ultra basis sets, and plane waves (PW); as well as two types of potential methods: norm-conserving Pseudo-Dojo pseudopotentials for both boron and arsenic, and the projector augmented-wave (PAW) method. The optimised Pseudo-Dojo pseudopotentials achieve a balance between computational efficiency and accuracy in the calculations, while PAW is a generalisation of pseudopotential and linear augmented-plane-wave methods, transforming rapidly oscillating wavefunctions near ion cores into smooth wavefunctions [31]. The DFT calculations with the PW basis set use a cut-off energy of 1088 eV (40 Ha), while the calculations with the LCAO basis set use a cut-off energy of 2857 eV (105 Ha), and the calculation with the PAW method uses a cut-off energy of 544 eV (20 Ha). More detailed results demonstrating the convergence of total energy in our DFT QATK calculations are presented in the Supplementary Material.

The QESP and VASP DFT calculations utilise the same lattice constant and the same **k**-point grid of $10 \times 10 \times 10$, but employ a cut-off energy of 1633 eV (60 Ha, 120 Ry) in QESP and 1000 eV (36.7 Ha, 73.5 Ry) in VASP. The atomic positions and lattice vectors of the primitive cell of the calculated structures in all DFT codes: QATK, QESP, and VASP, are relaxed at the level of the Perdew–Burke–Ernzerhof (PBE) functional [32] via the quasi-Newton algorithm (the Broyden–Fletcher–Goldfarb–Shanno algorithm in QESP) with a maximal interatomic force criterion of 10^{-5} eV/Å and a threshold of 0.01 GPa for the cell stress. In addition to the PBE and HSE06 simulations, we computed the electronic structure of cBAs using the recently developed TASK exchange functional [33], which we combined with the PW92 correlation functional. We also used the YAMBO code [34] to compute corrections to the PBE-level QESP bandstructures using G_0W_0 quasiparticle energies, which provide a theoretical reference for the intrinsic electronic structure of cBAs. A transferred momentum grid of $8 \times 8 \times 8$ **q**-points, 700 unoccupied bands, and a cut-off for the response function of 400 eV were employed in this step. We further modelled the frequency-dependence of the dielectric screening using the recently proposed [35] multipole approximation, where we found that the inclusion of 8 poles yields a good agreement with explicit full-frequency simulations using the contour deformation technique. To reduce effects from the atomic geometry, we used the experimental lattice constants for the calculation of the GW corrections. The GW corrections were then Wannier interpolated to the band path of interest and added to the PBE bandstructure. Based on our convergence tests [cf. Fig. S20 in the supplemental material], we expect our reported GW bandgaps to be converged to within 10 meV.

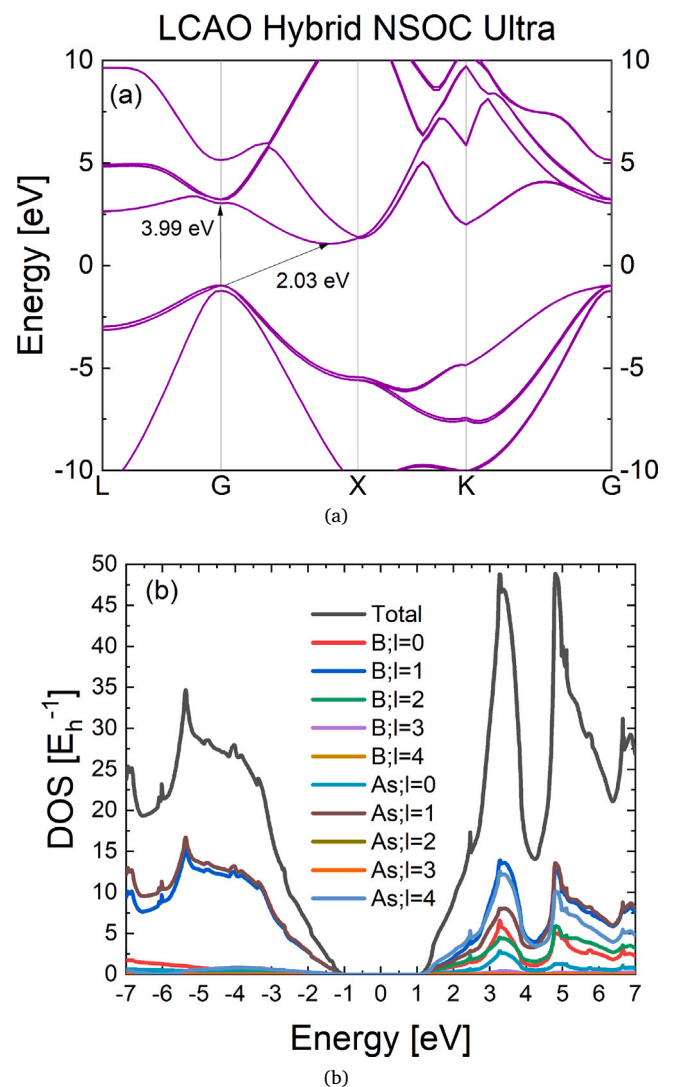
(a)

(b)

Fig. 4. (a) Bandstructure and (b) projected density of states of cBAs obtained using QATK calculations based on the LCAO, an ultra basis set, Pseudo-Dojo pseudopotentials, the hybrid HSE06 functional, and non-collinear SOC (NSOC).
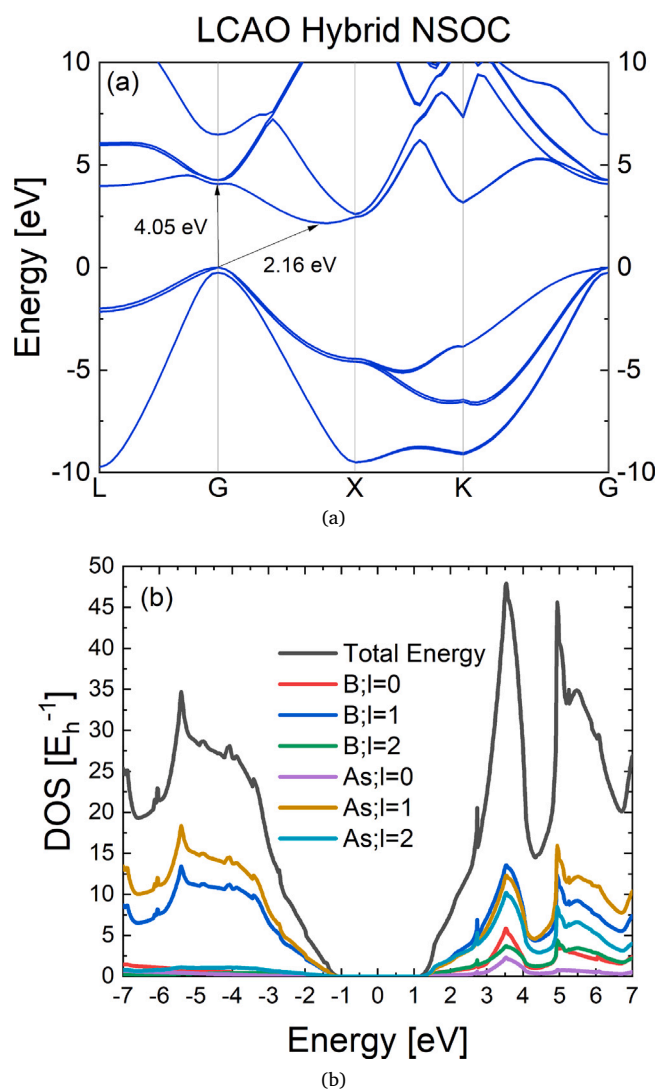
LCAO Hybrid NSOC

(a)

(b)

Fig. 5. (a) Bandstructure and (b) projected density of states (DoS) of cBAs, calculated using QATK with the LCAO, a medium basis set, Pseudo-Dojo pseudopotentials, the hybrid HSE06 functional, and non-collinear SOC (NSOC).

2.1. Application of density functional theory

We investigate two exchange–correlation DFT functionals, the crucial elements for bandstructure calculations within the DFT: the Perdew-Burke-Ernzerhof functional (GGA.PBE) [32], based on the generalised gradient approximation (GGA), and the hybrid Heyd–Scuseria–Ernzerhof 2006 (HSE06) [36] functional. The hybrid HSE06 functional includes 25% of Hartree–Fock exchange and 75% exchange from the PBE functional [32]. We assume non-collinear spin–orbit coupling (SOC), which is found to play an essential role in this relatively wide-bandgap semiconductor. Non-collinear spin polarisation means that electrons cannot just have spin up and spin down, but they can also have spin in any direction. This is particularly beneficial in non-magnetic materials such as cBAs, because spin polarisations can form orthogonal configurations. Additionally, by using non-collinear spin polarisation, we can correct for SOC, where some bands may split and slightly increase or decrease the bandgap energy. The Supplementary Material also contains the cBAs bandstructures obtained from the DFT calculations with unpolarised SOC for comparison.
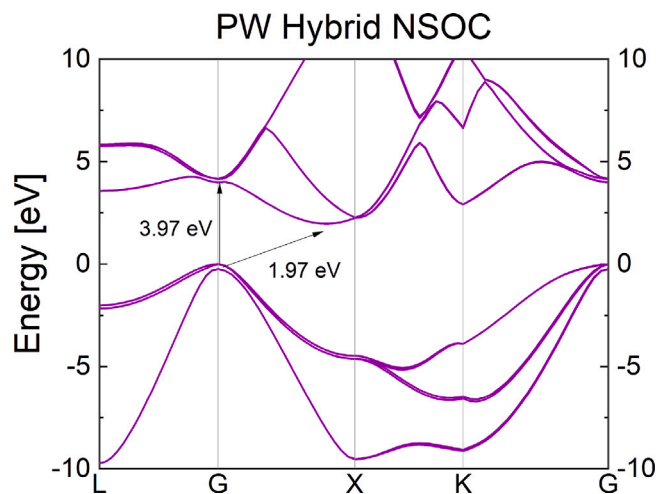
PW Hybrid NSOC

Fig. 6. Bandstructure of cBAs obtained from QATK using the PW basis set, the Pseudo-Dojo pseudopotential, the hybrid HSE06 functional, and non-collinear SOC (NSOC).

Table 1 collects the indirect and direct bandgaps for cBAs obtained from the bandstructures calculated using the optimised atomic structures as previously described. The accuracy of the bandgap energy, evaluated against the experimental data, is critically influenced by the approximation of the exchange–correlation energy. Specifically, when the exchange–correlation energy is approximated with the generalised gradient approximation (GGA) by using the PBE functional, the indirect and direct bandgaps of cBAs are systematically underestimated when compared against the experimental results in the range of 2.02 eV and 2.01 eV for the indirect bandgap, and of 4.12 eV and 4.24 eV for the direct bandgap. Fig. 2 shows that the LCAO basis set used with the GGA.PBE functional will give an underestimated indirect bandgap of 1.29 eV and an similarly underestimated direct bandgap of 3.16 eV. When the PW basis is selected with the GGA.PBE functional, the indirect bandgap of 1.12 eV and the direct bandgap of 3.08 eV are even more underestimated, as seen in Fig. 3. This bandgap underestimation remains largely unaffected by the replacement from non-collinear to unpolarised SOC, as is illustrated in Table S1 (Supplementary Material), and is a well-known property of LDA- and GGA-type functionals due to an absence of a derivative discontinuity in the exchange–correlation potential.

When the GGA.PBE functional is replaced by the hybrid HSE06 functional [36] as shown by bandstructures in Figs. 4(a), 5(a), and 6, the calculated indirect bandgap (E_G^{indir}) gets closer to its experimental value in the range of 1.97 eV and 2.16 eV, and the calculated direct bandgap (E_G^{dir}) to its experimental value in the range of 3.95 eV and 4.24 eV, obtained from the UV–Vis-NIR spectroscopy.

This remarkable improvement in the bandgaps calculations results from a more accurate approximation of the exchange–correlation self-energy. Hybrid functionals operate on the principle that the bandgap is primarily influenced by the screened exchange component of the potential [37]. The exchange–correlation potential is thus approximated by a spatially non-local operator, constructed from a functional that combines GGA with a fraction of exact Hartree–Fock exchange. Specifically, the HSE family of hybrid functionals employs one quarter of the Fock exchange operator, screened at long range to account for dielectric screening effects [20]. In general, our HSE06 bandgaps are quite close to the G_0W_0 results ($E_G^{indir} = 2.11\,\text{eV}$, $E_G^{dir} = 4.14\,\text{eV}$) presented in Fig. 7, highlighting the similar accuracy of hybrid functionals at a comparatively smaller computational cost. We note that the slight underestimation of the HSE06 bandgaps compared to G_0W_0 aligns well with the trend for other gapped materials [38].
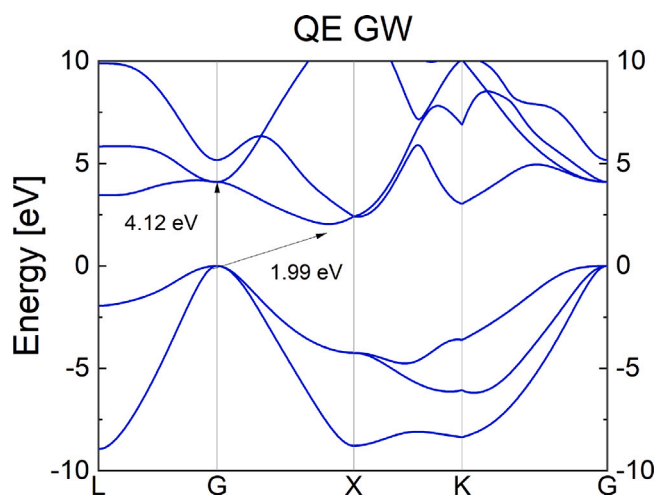
Fig. 7. Bandstructure of cBAs obtained from QESP (QE) calculated using a plane wave (PW) basis set, the Perdew–Burke–Ernzerhof (PBE) exchange–correlation functional with self-energy corrections obtained from a Green function (G) and screened Coulomb interaction (W) approach (GW), and without included SOC effects.
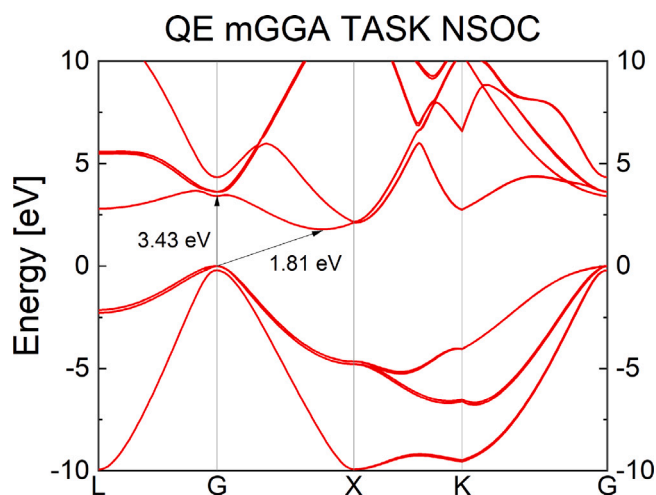

Fig. 8. Bandstructure of cBAs obtained from QESP (QE) calculated using the plane wave basis set, Pseudo-Dojo pseudopotentials, the TASK meta-GGA functional (mGGA), and non-collinear SOC.

We find that the best agreement with experiment is obtained when using the LCAO with an ultra basis set, together with the optimised, norm-conserving Pseudo-Dojo pseudopotentials, the hybrid HSE06 functional, and non-collinear spin. This DFT calculation approach gives an indirect bandgap of 2.03 eV and a direct bandgap of 3.99 eV, as illustrated in Fig. 4(a), which is consistent with other literature [12,14,39] and very close to our measured experimental values shown in Figs. 9 and 10, as well as to recent experimental data [28] collected in Table 2. Fig. 4(b) shows the projected density of states (DoS), illustrating the total energy and the individual orbital contributions from the two atoms, boron and arsenic. The major orbital contributions are from p-type orbitals ($l = 1$) of both boron and arsenide, as the valence band primarily originates from bonding between the valence orbitals of B and As in the zinc-blende structure of cBAs.

When the LCAO with an ultra basis set are replaced with the LCAO with a medium basis set in effort to reduce calculation time, the indirect bandgap increases to 2.16 eV and the direct bandgap to 4.05 eV as illustrated in Fig. 5(a). The ultra basis set thus does provide greater accuracy, even with a moderate increase in computational cost,

especially when compared with the PBE+GW approach. Fig. 5(b) shows the projected density of states (DoS) obtained from this DFT approach, which illustrates the system total energy and the individual orbital contributions from the constituent atoms, boron and arsenic.

When the LCAO basis sets are replaced with the PW set, the indirect bandgap decreases to 1.97 eV and the direct bandgap to 3.97 eV, as shown in the bandstructure in Fig. 6. Finally, Fig. 8 presents the cBAs bandstructure obtained from the recently developed TASK [33] meta-Generalised Gradient Approximation (meta-GGA) functional with the PW basis set, as recommended for meta-GGA Pseudo-Dojo pseudopotentials, and non-collinear SOC. Meta-GGA exchange–correlation functionals go beyond standard GGA by computing the kinetic energy density during the self-consistent field iterations, thus adding orbital level contributions. In the TASK functional, this increased flexibility was used to introduce exchange nonlocality and a derivative discontinuity into a meta-GGA form, yielding strongly improved bandgaps at essentially the computational cost of semi-local GGA functionals. We find that TASK indeed predicts larger direct and indirect bandgaps for cBAs compared to our GGA simulations, but falls short of the accuracy of HSE06.

The SOC change from the more physically realistic, non-collinear SOC to a less realistic, unpolarised SOC, consistently increases the indirect bandgap from 2.16 eV to 2.24 eV when using the hybrid HSE06 functional with the LCAO medium basis set. Similarly, when using the hybrid HSE06 functional with the PW basis set, the indirect bandgap increases from 1.97 eV to 2.05 eV and the direct bandgap from 3.97 eV to 4.2 eV, as is presented in Table S1 (Supplementary Material). This increase of the bandgaps towards energies closer to the experimental data confirms that the use of the hybrid HSE06 functional is an essential choice to achieve more realistic bandstructure calculations. This is further confirmed when norm-conserving Pseudo-Dojo pseudopotentials are replaced by the physically more accurate PAW method. The indirect and direct bandgaps remain practically unchanged, with an indirect bandgap of 1.13 eV and a slightly decreased direct bandgap of 3.04 eV.

3. Experimental bandgap from infrared spectroscopy

Fabrication of large, high-quality single crystals of cBAs is known to be very challenging, as precise control of the nucleation process is critical to grow large, high-quality crystals. This is because tiny defects in the quartz tube used for growth can cause spontaneous nucleation. These random nucleation sites lead to irregular morphology and micro-cracks in the final crystals [45]. Progress was made in 2018 utilising a seeded Chemical Vapour Transport (CVT) technique. Small cBAs crystals a few microns long where used to ensure the nucleation centres were under control [46]. This process allowed the growth of millimetre sized crystals.

The bandgap measurements of cBAs are carried out by UV–Vis-NIR spectroscopy [30]. Our UV–Vis-NIR spectroscopy measurements use a pinhole spectrophotometer with a 500 μm opening and a crossover wavelength of 900 nm. The absorption is measured without the sample in place to obtain a baseline absorption level. This baseline is then subtracted from the absorption with the sample in place in order to more accurately determine the indirect and direct bandgaps, as shown in Figs. 9 and 10, respectively. However, the extraction of the indirect bandgap is not straightforward because the cBAs crystal still contains imperfections from the particular growth technique, CVT [39,47], such as point defects and common impurities like carbon and silicon [41], resulting in hole conduction. The contribution of these imperfections into the measured absorption can be removed by assuming that the absorption coefficient α_{total} constitutes of two contributions from a perfect crystal and the imperfections as: $\alpha_{total} = \alpha_{crystal} + \alpha_{imperfections}$ [28]. Fig. 9 illustrates that if the absorption coefficient is given by [48]: $\alpha = A\left(h\nu - E_G\right)$, where A is a constant, $h\nu$ is the phonon energy, and E_G is the material bandgap, then the absorption coefficient must be linearly dependent on the phonon energy [28]. Therefore, the indirect bandgap

Table 2

A collection of indirect and direst cBAs bandgaps from the literature, obtained experimentally and from DFT calculations, using a variety of approximate methods. LT-PL stands for the low temperature photoluminescence, UV–Vis for ultraviolet–visible spectroscopy, UV–Vis-NIR for ultraviolet–visible-near infrared spectroscopy, STS for scanning tunnelling spectroscopy, VASP for the Vienna Ab-initio Simulation Package, GAMESS for the General Atomic and Molecular Electronic Structure System, GGA.PBE for the Perdew–Burke–Ernzerhof (PBE) functional – a common choice within the generalised gradient approximation (GGA), HSE for the hybrid Heyd–Scuseria–Ernzerhof functional, LDA for the local-density approximation, and GW for the G_0W_0 method, which uses the non-interacting Green's function (G_0) and the screened Coulomb interaction (W_0), calculated without solving the Dyson equation self-consistently. PAW is the projector augmented-wave method, LCGO stands for the linear combination of Gaussian orbitals, and LCAO for the linear combination of atomic orbitals.

| Method	Indirect bandgap [eV]	Direct bandgap [eV]	Reference
Experimental: UV–Vis	1.46	N/A	[40]
Experimental: LT-PL	1.78	3.95	[41]
Experimental: UV–Vis	1.82	N/A	[12]
Experimental: STS	2.1	N/A	[14]
Experimental: idealised UV–Vis	1.835	N/A	[42]
Experimental: UV–Vis-NIR	2.02	4.12	[28]
Experimental: UV–Vis-NIR	2.01	4.24	This work
Calculations: VASP, GGA.PBE	0.98	N/A	[13]
Calculations: VASP, HSE	2.05	N/A	[14]
Calculations: VASP, HSE06, PAW	1.78	N/A	[41]
Calculations: QESP, LDA, GW	2.07	4.25	[28]
Calculations: QESP, LDA, GW	2.049	4.135	[43]
Calculations: GAMESS, LDA, LCGO	1.48	3.3	[44]
Calculations: QATK, HSE06, LCAO	2.03	3.99	This work
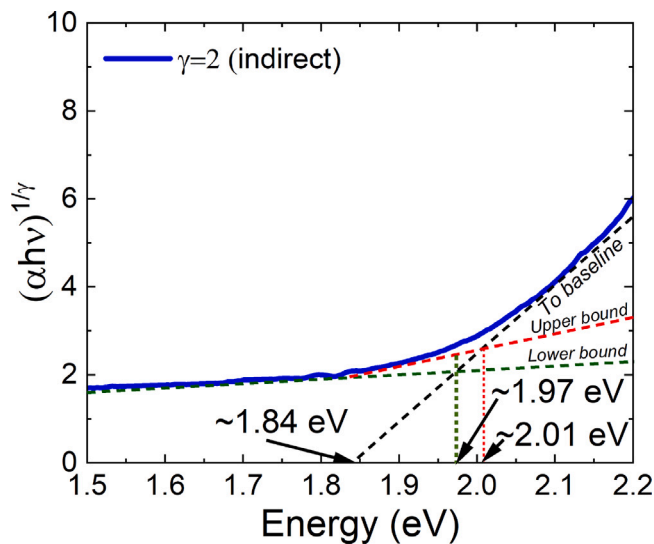
Fig. 9. The square root of the absorption coefficient (blue line) as a function of photon energy, used to determine the indirect bandgap of cBAs using UV–Vis-NIR spectroscopy. The absorption contains contributions from the crystal (black dash line), indicated by baseline, and imperfections, indicated by lower and upper bounds (green and red dashed lines), which appear as background signals. The crystal bandgap is identified at the intersection of the upper bound (red dashed line), where impurity effects begin, and the baseline. The lower bound (green dashed line) is shown for comparison.

Fig. 10. The square root of the absorption coefficient as a function of photon energy is used to determine an direct bandgap of cBAs using UV–Vis-NIR spectroscopy. Similar to the determination of the indirect bandgap (Fig. 9), the absorption includes contributions from both the crystal itself (black dashed line) and imperfections (upper bounds), which manifest as background signals. The crystal bandgap is determined at the crossing of the upper bound (red dashed line), indicating the onset of impurities, and the baseline.

of a perfect crystal, calculated by the DFT method, can be determined from the point where the slope of the absorption changes [28], as shown in Fig. 9. The extracted indirect bandgap is 2.01 eV, which is also in line with experimental data from the literature as summarised in Table 2. The measured absorption coefficient for the direct bandgap indicates negligible imperfections, exhibiting a distinct transition at the band edge, leading to an extracted direct bandgap of 4.24 eV, as illustrated in Fig. 10. We would like to note that the signal-to-noise ratio of the absorption data is low due to the small sample size. Therefore, the optical bandgap extracted from this method is subject to experimental uncertainty. Nonetheless, the extracted indirect and direct bandgaps align well with values reported in the literature [28].
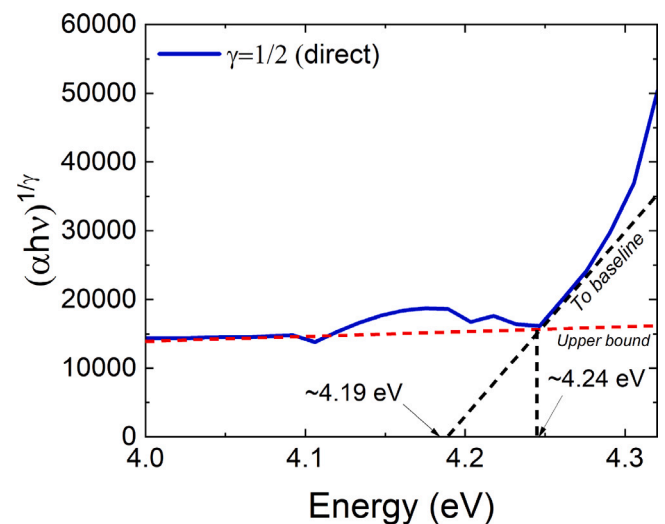
4. Conclusion

The systematic study of the various DFT calculation approaches within three DFT codes has been carried out to obtain the bandstructure of cBAs. The main criterion for accuracy is the indirect and direct bandgaps extracted from the UV–Vis-NIR spectroscopy measurements, as well as previous experimental measurements [28]. We have employed one commercial DFT code, QATK (Synopsys) [15], and two open source DFT codes, QESP and VASP, exploring basis sets like PW and medium/ultra LCAO, potentials like Pseudo-Dojo pseudopotential and PAW, and comparing three exchange–correlation energy functionals: GGA.PBE, meta-GGA, and HSE06. We have also studied the effect of SOC using non-collinear, collinear, and unpolarised SOC.

The greatest accuracy in bandgap DFT calculations is obtained when using the LCAO with an ultra basis set, the hybrid HSE06 functional, Pseudo-Dojo pseudopotentials, and non-collinear SOC within QATK, giving an indirect bandgap of 2.03 eV and a direct bandgap of 3.99 eV. This is in line with a reported DFT value of 2.07 eV and 4.25 eV [28] and 2.049 eV and 4.135 eV [43], and in excellent agreement with our measured indirect and direct bandgaps of 2.01 eV and 4.24 eV, as well as recent experimental values of 2.02 eV and 4.12 eV [28], respectively. The exploration of alternative DFT approaches, as collected in Table 1, shows indirect bandgaps between 1.13 eV and 2.16 eV, and direct bandgaps between 3.04 eV and 4.05 eV. The study demonstrates that non-collinear SOC is an essential ingredient of the physically meaningful bandstructure calculations in relatively wide bandgap materials. A very low value of 0.98 eV [13] was reported by using the GGA exchange–correlation potential, which is known to underestimate bandgaps. This is consistent with our result of 1.16 eV using the same exchange–correlation functional. The use of the hybrid exchange–correlation HSE06 functional increases the bandgaps to 2.03 eV and 3.99 eV (see Fig. 4(a)), highlighting the importance of both the HSE06 functional and optimised PseudoDojo pseudopotentials in achieving reliable results.

CRediT authorship contribution statement

A. King: Writing – review & editing, Writing – original draft, Visualization, Data curation. **R. Gillen:** Writing – review & editing, Data curation. **G. Burwell:** Writing – review & editing, Formal analysis, Data curation. **B.A. Niyikiza:** Resources. **F.J. Pan:** Resources. **Z.F. Ren:** Writing – review & editing, Resources. **L. Li:** Writing – review & editing, Supervision, Methodology. **K. Kalna:** Writing – review & editing, Writing – original draft, Supervision, Project administration, Funding acquisition, Formal analysis, Conceptualization.

Declaration of competing interest

The authors declare the following financial interests/personal relationships which may be considered as potential competing interests: Given Zhifeng Ren's role as Editor-in-Chief of Materials Today Physics, Zhifeng Ren had no involvement in the peer review of this article and had no access to information regarding its peer review. Full responsibility for the editorial process for this article was delegated to another journal editor. If there are other authors, they declare that they have no known competing financial interests or personal relationships that could have appeared to influence the work reported in this paper.

Acknowledgements

Appendix A. Supplementary data

Supplementary material related to this article can be found online at https://doi.org/10.1016/j.mtphys.2025.101962.

Data availability

Data will be made available on request.

References

[1] F. Tian, B. Song, X. Chen, N.K. Ravichandran, Y. Lv, K. Chen, S. Sullivan, J. Kim, Y. Zhou, T.-H. Liu, M. Goni, Z. Ding, J. Sun, G.A.G.U. Gamage, H. Sun, H. Ziyaee, S. Huyan, L. Deng, J. Zhou, A.J. Schmidt, S. Chen, C.-W. Chu, P.Y. Huang, D. Broido, L. Shi, G. Chen, Z. Ren, Unusual high thermal conductivity in boron arsenide bulk crystals, Science 361 (6402) (2018) 582–585, http://dx.doi.org/10.1126/science.aat7932.

[2] S. Li, Q. Zheng, Y. Lv, X. Liu, X. Wang, P.Y. Huang, D.G. Cahill, B. Lv, High thermal conductivity in cubic boron arsenide crystals, Science 361 (6402) (2018) 579–581, http://dx.doi.org/10.1126/science.aat8982.

[3] H.-S. Wong, D. Frank, P. Solomon, C. Wann, J. Welser, Nanoscale CMOS, Proc. IEEE 87 (4) (1999) 537–570, http://dx.doi.org/10.1109/5.752515.

[4] H.-S.P. Wong, Beyond the conventional transistor, IBM J. Res. Dev. 46 (2.3) (2002) 133–168, http://dx.doi.org/10.1147/rd.462.0133.

[5] J. Uyemura, Circuit Design for CMOS VLSI, Kluwer Academic Publishers, 1992.

[6] S. Biasco, F. Burri, S. Houver, E. Abreu, M. Savoini, S.L. Johnson, Impact ionization in low-band-gap semiconductors driven by ultrafast terahertz excitation: Beyond the ballistic regime, Phys. Rev. B 106 (2022) 235201, http://dx.doi.org/10.1103/PhysRevB.106.235201.

[7] K. Kalna, A. Asenov, Gate tunnelling and impact ionisation in sub 100 nm PHEMTs, in: Int. Conf. Simulation of Semiconductor Processes and Devices, 2002, pp. 139–142, http://dx.doi.org/10.1109/SISPAD.2002.1034536.

[8] K. Kalna, A. Asenov, Role of multiple delta doping in PHEMTs scaled to sub-100 nm dimensions, Solid St. Electron. 48 (7) (2004) 1223–1232, http://dx.doi.org/10.1016/j.sse.2004.02.008.

[9] R. Gaska, A. Osinsky, J. Yang, M. Shur, Self-heating in high-power AlGaN-GaN HFETs, IEEE Electron Device Lett. 19 (3) (1998) 89–91, http://dx.doi.org/10.1109/55.661174.

[10] S.J. Pearton, J. Yang, I. Cary, F. Ren, J. Kim, M.J. Tadjer, M.A. Mastro, A review of Ga₂O₃ materials, processing, and devices, Appl. Phys. Rev. 5 (1) (2018) 011301, http://dx.doi.org/10.1063/1.5006941.

[11] J. Shin, G.A. Gamage, Z. Ding, K. Chen, F. Tian, X. Qian, J. Zhou, H. Lee, J. Zhou, L. Shi, T. Nguyen, F. Han, M. Li, D. Broido, A. Schmidt, Z. Ren, G. Chen, High ambipolar mobility in cubic boron arsenide, Science 377 (6604) (2022) 437–440, http://dx.doi.org/10.1126/science.abn4290.

[12] J.S. Kang, M. Li, H. Wu, H. Nguyen, Y. Hu, Basic physical properties of cubic boron arsenide, Appl. Phys. Lett. 115 (12) (2019) 122103, http://dx.doi.org/10.1063/1.5116025.

[13] Z. Fu, H. Guo, X. Wang, R. Cao, H. Zhong, S. Liu, J. Robertson, Y. Guo, Z. Zhang, Metal contacts and schottky barrier heights at boron arsenide interfaces: A first-principles study, J. Appl. Phys. 134 (11) (2023) 115302, http://dx.doi.org/10.1063/5.0163908.

[14] H. Lee, G.A. Gamage, J.L. Lyons, F. Tian, B. Smith, E.R. Glaser, Z. Ren, L. Shi, Electronic structure of cubic boron arsenide probed by scanning tunneling spectroscopy, J. Phys. D: Appl. Phys. 54 (31) (2021) 251902.

[15] S. Smidstrup, K. Stokbro, A. Blom, T. Markussen, J. Wellendorff, J. Schneider, T. Gunst, B. Verstichel, P.A. Khomyakov, U.G. Vej-Hansen, M. Brandbyge, K. Stokbro, QuantumATK: An integrated platform of electronic and atomic-scale modelling tools, J. Phys: Condens. Matter (APS) 32 (2020) 015901, http://dx.doi.org/10.1088/1361-648X/ab4007.

[16] P. Giannozzi, S. Baroni, N. Bonini, M. Calandra, R. Car, C. Cavazzoni, D. Ceresoli, G.L. Chiarotti, M. Cococcioni, I. Dabo, A.D. Corso, S. de Gironcoli, S. Fabris, G. Fratesi, R. Gebauer, U. Gerstmann, C. Gougoussis, A. Kokalj, M. Lazzeri, L. Martin-Samos, N. Marzari, F. Mauri, R. Mazzarello, S. Paolini, A. Pasquarello, L. Paulatto, C. Sbraccia, S. Scandolo, G. Sclauzero, A.P. Seitsonen, A. Smogunov, P. Umari, R.M. Wentzcovitch, QUANTUM ESPRESSO: a modular and open-source software project for quantum simulations of materials, J. Phys.: Condens. Matter. 21 (39) (2009) 395502, http://dx.doi.org/10.1088/0953-8984/21/39/395502.

[17] G. Kresse, J. Hafner, Ab initio molecular dynamics for liquid metals, Phys. Rev. B 47 (1993) 558–561, http://dx.doi.org/10.1103/PhysRevB.47.558.

[18] G. Kresse, J. Furthmüller, Efficient iterative schemes for ab initio total-energy calculations using a plane-wave basis set, Phys. Rev. B 54 (1996) 11169–11186, http://dx.doi.org/10.1103/PhysRevB.54.11169.

[19] I.N. Remediakis, E. Kaxiras, Band-structure calculations for semiconductors within generalized-density-functional theory, Phys. Rev. B 59 (1999) 5536–5543, http://dx.doi.org/10.1103/PhysRevB.59.5536.

[20] F. Bechstedt, F. Fuchs, G. Kresse, Ab-initio theory of semiconductor band structures: New developments and progress, Phys. Status Solidi (B) 246 (8) (2009) 1877–1892, http://dx.doi.org/10.1002/pssb.200945074.

[21] A. Belabbes, C. Panse, J. Furthmüller, F. Bechstedt, Electronic bands of III-v semiconductor polytypes and their alignment, Phys. Rev. B 86 (2012) 075208, http://dx.doi.org/10.1103/PhysRevB.86.075208.

[22] L. Hedin, New method for calculating the one-particle green's function with application to the electron-gas problem, Phys. Rev. 139 (1965) A796–A823, http://dx.doi.org/10.1103/PhysRev.139.A796.

[23] S.J. Clark, J. Robertson, Calculation of semiconductor band structures and defects by the screened exchange density functional, Phys. Status Solidi b 248 (3) (2011) 537–546, http://dx.doi.org/10.1002/pssb.201046110.

[24] L. Li, Piezoelectric properties of substitutionally doped β-Ga_2O_3, AIP Adv. 11 (6) (2021) 065111, http://dx.doi.org/10.1063/5.0048975.

[25] R. Baer, E. Livshits, U. Salzner, Tuned range-separated hybrids in density functional theory, Annu. Rev. Phys. Chem. 61 (2010) 85–109, http://dx.doi.org/10.1146/annurev.physchem.012809.103321.

[26] M.-Y. Zhang, Z.-H. Cui, Y.-C. Wang, H. Jiang, Hybrid functionals with system-dependent parameters: Conceptual foundations and methodological developments, WIRES Comput. Mol. Sci. 10 (6) (2020) e1476, http://dx.doi.org/10.1002/wcms.1476.

[27] N. Mardirossian, M. Head-Gordon, Thirty years of density functional theory in computational chemistry: an overview and extensive assessment of 200 density functionals, Mol. Phys. 115 (19) (2017) 2315–2372, http://dx.doi.org/10.1080/00268976.2017.1333644.

[28] B. Song, K. Chen, K. Bushick, K.A. Mengle, F. Tian, G.A.G.U. Gamage, Z. Ren, E. Kioupakis, G. Chen, Optical properties of cubic boron arsenide, Appl. Phys. Lett. 116 (14) (2020) 141903, http://dx.doi.org/10.1063/5.0004666.

[29] J. Heyd, G.E. Scuseria, M. Ernzerhof, Hybrid functionals based on a screened Coulomb potential, J. Chem. Phys. 118 (18) (2003) 8207–8215, http://dx.doi.org/10.1063/1.1564060.

[30] G.F. Kortüm, Reflectance Spectroscopy: Principles, Methods, Applications, Springer-Verlag, Heidelberg, 1969, http://dx.doi.org/10.1007/978-3-642-88071-1.

[31] P.E. Blöchl, Projector augmented-wave method, Phys. Rev. B 50 (1994) 17953–17979, http://dx.doi.org/10.1103/PhysRevB.50.17953.

[32] J.P. Perdew, K. Burke, M. Ernzerhof, Generalized gradient approximation made simple, Phys. Rev. Lett. 78 (1997) 1396–1396, http://dx.doi.org/10.1103/PhysRevLett.78.1396.

[33] T. Lebeda, T. Aschebrock, J. Sun, L. Leppert, S. Kümmel, Right band gaps for the right reason at low computational cost with a meta-GGA, Phys. Rev. Mater. 7 (2023) 093803, http://dx.doi.org/10.1103/PhysRevMaterials.7.093803.

[34] A. Marini, C. Hogan, M. Grüning, D. Varsano, Yambo: An ab initio tool for excited state calculations, Comp. Phys. Commun. 180 (8) (2009) 1392–1403, http://dx.doi.org/10.1016/j.cpc.2009.02.003.

[35] D.A. Leon, C. Cardoso, T. Chiarotti, D. Varsano, E. Molinari, A. Ferretti, Frequency dependence in GW made simple using a multipole approximation, Phys. Rev. B 104 (2021) 115157, http://dx.doi.org/10.1103/PhysRevB.104.115157.

[36] A.V. Krukau, O.A. Vydrov, A.F. Izmaylov, G.E. Scuseria, Influence of the exchange screening parameter on the performance of screened hybrid functionals, J. Chem. Phys. 125 (22) (2006) 224106, http://dx.doi.org/10.1063/1.2404663.

[37] J. Heyd, G.E. Scuseria, M. Ernzerhof, Hybrid functionals based on a screened Coulomb potential, J. Chem. Phys. 118 (18) (2003) 8207–8215, http://dx.doi.org/10.1063/1.1564060.

[38] W. Chen, A. Pasquarello, Band-edge levels in semiconductors and insulators: Hybrid density functional theory versus many-body perturbation theory, Phys. Rev. B 86 (2012) 035134, http://dx.doi.org/10.1103/PhysRevB.86.035134.

[39] S. Chae, K. Mengle, J.T. Heron, E. Kioupakis, Point defects and dopants of boron arsenide from first-principles calculations: Donor compensation and doping asymmetry, Appl. Phys. Lett. 113 (21) (2018) 212101, http://dx.doi.org/10.1063/1.5062267.

[40] S. Wang, S.F. Swingle, H. Ye, F.-R.F. Fan, A.H. Cowley, A.J. Bard, Synthesis and characterization of a p-type boron arsenide photoelectrode, J. Am. Chem. Soc. 134 (27) (2012) 11056–11059, http://dx.doi.org/10.1021/ja301765v.

[41] J.L. Lyons, J.B. Varley, E.R. Glaser, J. Freitas, J.C. Culbertson, F. Tian, G.A. Gamage, H. Sun, H. Ziyaee, Z. Ren, Impurity-derived p-type conductivity in cubic boron arsenide, Appl. Phys. Lett. 113 (25) (2018) 251902, http://dx.doi.org/10.1063/1.5058134.

[42] H. Zhong, F. Pan, S. Yue, C. Qin, V. Hadjiev, F. Tian, X. Liu, F. Lin, Z. Wang, J. Bao, Idealizing Tauc plot for accurate bandgap determination of semiconductor with ultraviolet–Visible spectroscopy: A case study for cubic boron arsenide, J. Phys. Chem. Lett. 14 (29) (2023) 6702–6708, http://dx.doi.org/10.1021/acs.jpclett.3c01416.

[43] K. Bushick, K. Mengle, N. Sanders, E. Kioupakis, Band structure and carrier effective masses of boron arsenide: Effects of quasiparticle and spin-orbit coupling corrections, Appl. Phys. Lett. 114 (2) (2019) 022101, http://dx.doi.org/10.1063/1.5062845.

[44] I.H. Nwigboji, Y. Malozovsky, L. Franklin, D. Bagayoko, Calculated electronic, transport, and related properties of zinc blende boron arsenide (zb-BAs), J. Appl. Phys. 120 (14) (2016) 145701, http://dx.doi.org/10.1063/1.4964421.

[45] F. Tian, B. Song, B. Lv, J. Sun, S. Huyan, Q. Wu, J. Mao, Y. Ni, Z. Ding, S. Huberman, T.-H. Liu, G. Chen, S. Chen, C.-W. Chu, Z. Ren, Seeded growth of boron arsenide single crystals with high thermal conductivity, Appl. Phys. Lett. 112 (3) (2018) 031903, http://dx.doi.org/10.1063/1.5004200.

[46] F. Tian, B. Song, X. Chen, N.K. Ravichandran, Y. Lv, K. Chen, S. Sullivan, J. Kim, Y. Zhou, T.-H. Liu, M. Goni, Z. Ding, J. Sun, G.A.G.U. Gamage, H. Sun, H. Ziyaee, S. Huyan, L. Deng, J. Zhou, A.J. Schmidt, S. Chen, C.-W. Chu, P.Y. Huang, D. Broido, L. Shi, G. Chen, Z. Ren, Unusual high thermal conductivity in boron arsenide bulk crystals, Science 361 (6402) (2018) 582–585, http://dx.doi.org/10.1126/science.aat7932.

[47] Q. Zheng, C.A. Polanco, M.-H. Du, L.R. Lindsay, M. Chi, J. Yan, B.C. Sales, Antisite pairs suppress the thermal conductivity of BAs, Phys. Rev. Lett. 121 (2018) 105901, http://dx.doi.org/10.1103/PhysRevLett.121.105901.

[48] J. Tauc, Optical properties and electronic structure of amorphous Ge and Si, Mater. Res. Bull. 3 (1) (1968) 37–46, http://dx.doi.org/10.1016/0025-5408(68)90023-8.